


Highly Efficient Photoelectrochemical Water Oxidation Using $\text{Cs}_2\text{AgMCl}_6$ ($M = \text{In, Bi, Sb}$) Halide Double Perovskites

Poonam Sikarwar,¹ Indrajith Thirvikram Koneri,¹ Tamilselvan Appadurai,¹ and Aravind Kumar Chandiran^{1,2,*}

¹Department of Chemical Engineering, Indian Institute of Technology Madras, Adyar, Chennai, Tamil Nadu 600036, India

²Centre for Photo- and Electro-Chemical Energy, Indian Institute of Technology Madras, Adyar, Chennai, Tamil Nadu 600036, India

 (Received 7 April 2022; revised 11 March 2023; accepted 15 March 2023; published 26 April 2023)

In this work, stable $\text{Cs}_2\text{AgMCl}_6$ ($M = \text{Bi, In, Sb}$) double perovskite materials are successfully employed as photoanodes for solar water oxidation. These materials show an extraordinary oxidative stability, where $\text{Cs}_2\text{AgInCl}_6$ and $\text{Cs}_2\text{AgBiCl}_6$ are stable between 0 and 1.2 V (vs Ag-AgCl) and $\text{Cs}_2\text{AgSbCl}_6$ between 0 and 0.75 V (vs Ag-AgCl) over 100 cycles of electrochemical cycling. This enables us to employ these materials for photoelectrochemical (PEC) water oxidation in CH_3CN and H_2O , with and without IrO_x cocatalyst. All three materials show PEC activity, with $\text{Cs}_2\text{AgInCl}_6$ showing the highest performance. At 1.23 V (vs a reversible hydrogen electrode), a photocurrent density of 0.5 mA cm^{-2} is observed, and with an applied overpotential of 600 mV, the photocurrent increases to about 0.75 mA cm^{-2} . From the band gap of $\text{Cs}_2\text{AgInCl}_6$, the estimated theoretical maximum current is around 0.82 mA cm^{-2} . So, $\text{Cs}_2\text{AgInCl}_6$ -coated IrO_x gives nearly 60% and about 90% of the theoretical maximum photocurrent at zero bias and at an applied overpotential, respectively. The device is shown to be stable and reproducibility is confirmed.

DOI: [10.1103/PhysRevApplied.19.044083](https://doi.org/10.1103/PhysRevApplied.19.044083)

I. INTRODUCTION

Photoelectrochemical (PEC) water splitting is a sustainable way to store solar energy in the form of chemical fuels. A good photovoltaic material is a good candidate for solar water splitting provided criteria like stability in electrolyte medium and water-oxidation or -reduction catalytic capabilities are met [1,2]. In the last decade, halide perovskites have attracted a lot of attention among the photovoltaics community because they demonstrate a high photovoltaic power-conversion efficiency (PCE). Dye-sensitized-type photoelectrochemical regenerative solar cells with perovskite absorbers $\text{CH}_3\text{NH}_3\text{PbBr}_3$ and $\text{CH}_3\text{NH}_3\text{PbI}_3$ show a PCE of over 3.2%. The same class of materials has now reached greater than 20% PCE in solid-state solar cells [3–7].

These materials possess excellent optoelectronic properties like a high light-absorption coefficient, small exciton binding energy, good carrier lifetime, and charge-transport properties, and thus, these materials show an extraordinary PCE and, eventually, they are the right choice for PEC water-splitting materials [8–10]. However, the instability of these materials in electrolytes restricts them from being employed in PEC applications. The moment these

materials come in direct contact with moisture and oxygen, they decompose [11,12]. There are several reports stating that $\text{MAPb}(\text{Br}_x\text{I}_{1-x})_3$ (MA corresponds to methyl ammonium) shows long-term stability for over hundreds of hours in an ambient atmosphere under dark conditions but degrades immediately when exposed to moisture [12–16]. The use of a protection or passivation layer with a perovskite is employed for photoelectrochemical water splitting. Protecting layers like Ni, a field metal, carbon paste, mesoporous carbon with graphite sheets, titanium metal introduced by pulsed laser deposition, and atomic-layer-deposited (ALD) titanium dioxide are reported [17–22]. Almost all these devices take a solar-cell configuration with photoanodes containing TCO/ETL/perovskite/HTL/metal contact/protection layers/catalyst (configuration 1) and photocathodes taking the inverted design with TCO/HTL/perovskite/ETL/metal contact/protection layers/catalyst (configuration 2), where TCO is transparent conducting-oxide-coated glass, ETL is an electron-transport layer, and HTL is a hole-transport layer.

The nickel protection layer is deposited by magnetron sputtering on top of the perovskite solar cell with configuration 1, and it is used as a photoanode. Similar nickel protection coupled with surface passivation on perovskites using organic linkers enables solar water oxidation [23]. In another report, a combination of

*aravindkumar@iitm.ac.in

protection layers with a field metal and electrodeposited nickel is coated by a lift-off process, and the rest of the device is sealed using an epoxy sealant [18]. On top of the perovskite, three-layer protection with screen-printed carbon (graphite) slurry, conductive carbon, and silver paste is used [20]. A CsPbBr_3 photoanode protected with a thermal graphite sheet and mesoporous carbon scaffold is also shown to be an efficient protection strategy [21].

Configuration 2 with field-metal protection and a UV-curing resin is used as the protective layers along with a platinum catalyst for solar hydrogen production [24]. Another inverted device with aluminum-doped zinc oxide, a field metal, and a platinum catalyst with glue is also used as the photocathodes [25]. Similarly, field metal alloy with electrodeposited platinum is also used as a protecting layer [26]. The silver conductive paste on titanium foil and Pt, and eventually covered with glue, is reported to enhance the protection [27]. Pinhole-free ALD TiO_2 and a platinum layer also act as a protective photocathode [28]. In one recent study, at least four protection layers were deposited on the back contact for solar hydrogen production. The total number of layers in all the aforementioned devices varies between six and nine [22]. Although these devices work, the complexity in fabricating multilayer electrodes and the possibility of the creation of pinholes in the protecting layers can be detrimental to the device performance and stability. Ideally, a stable semiconductor with simple fabrication is preferred to carry out solar water splitting.

In 2020, bare vacancy-ordered halide perovskite Cs_2PtI_6 was reported as one of the most stable photoanodes for PEC water oxidation with a photocurrent of 0.8 mA cm^{-2} at 1.23 V versus a reversible hydrogen electrode (RHE) [29]. A halide double perovskite with formula $A_2MM'X_6$ is shown to be extremely stable under ambient conditions, unlike conventional AMX_3 systems. $\text{Cs}_2\text{AgBiBr}_6$ is a widely explored material in solar cells, where the PCE is shown to be about 3% [12,30,31]. This material is also employed for photocatalytic hydrogen evolution in aqueous HBr (or HBr and H_3PO_2) by forming a composite of $\text{Cs}_2\text{AgBiBr}_6$ with reduced graphene oxide [32,33]. $\text{Cs}_2\text{AgBiBr}_6$ is also explored for CO_2 reduction [34]. The tunability in optical and electronic properties that these materials offer, via four different cationic and anionic sites coupled with good ambient stability, makes this class of material an attractive candidate for PEC reaction.

Here, we explore one such stable halide double perovskite system with the formula $\text{Cs}_2\text{AgMCl}_6$, ($M = \text{Bi, In, Sb}$) for PEC water oxidation. The advantage of moving to the chloride, compared with the well-explored bromide compounds, is that the former has a more positive oxidation potential and is expected to give better oxidative stability for PEC oxidation reactions. The redox processes upon electrochemical cycling and the electrochemical stability window of the halide perovskite materials are investigated. Following an understanding of the

electrochemical properties, they are employed as photoanodes in PEC devices, and their water-oxidation capabilities are explored.

II. RESULTS AND DISCUSSION

Three different halide double perovskites, $\text{Cs}_2\text{AgInCl}_6$ (CAIC), $\text{Cs}_2\text{AgBiCl}_6$ (CABC), and $\text{Cs}_2\text{AgSbCl}_6$ (CASbC), are synthesized through a hydrothermal method. Detailed experimental procedures are given in Sec. IV. To employ these materials in electrochemical or photoelectrochemical devices, they should be stable in the electrolyte medium. To investigate their stability, these materials are separately added to aqueous and nonaqueous (dichloromethane and acetonitrile) solvents and left in the same medium for 2 h. After filtration and drying, their phase stability is characterized using x-ray diffraction (Fig. 1). In dichloromethane (DCM) and acetonitrile (ACN), the XRD patterns of all three materials remain similar to those of the as-synthesized compounds. However, in an aqueous medium, new peaks appear, indicating decomposition of the materials. Also, a color change from yellow to white is observed for CABC and CASbC in an aqueous medium, but no such change is observed for nonaqueous solvents (Fig. S1 within the Supplemental Material [35]). These results show that the double perovskites are stable in acetonitrile and dichloromethane but not in water. So, to understand their redox properties, electrochemical experiments are carried out in nonaqueous solvents.

The films of these perovskite materials are deposited on transparent conducting glass by either electrophoretic deposition (XRD patterns and SEM micrographs are given in Figs. S2 and S3 within the Supplemental Material [35]) or spin-coating methods and used as working electrodes (Figs. S4–S6 within the Supplemental Material [35]). The cyclic voltammetric (CV) measurements are carried out using Ag-AgCl (in saturated KCl) as a reference electrode, platinum coil as a counter electrode, and tetrabutylammonium hexafluorophosphate (TBAPF₆) in DCM as an electrolyte. All the voltages given hereafter are referenced to Ag-AgCl (sat.), unless stated otherwise. Figures 2(a)–2(c) show the cyclic voltammograms (0 V → 1 V → −1 V → 0 V) of CAIC, CABC, and CASbC, where (i) no oxidation signatures are observed within the range of 0–1 V in both forward and reverse scans for CAIC and CABC; (ii) for CASbC, the material starts oxidizing beyond 0.75 V [Fig. 2(c), inset]; and (iii) prominent reduction currents are observed in all the three materials between 0 and −1 V.

The changes in the materials due to the applied bias in CV measurements are investigated using FT-far-IR and x-ray photoelectron spectroscopic techniques. The IR spectra of the redox process at points 1, 2, and 3 in the cyclic voltammograms are shown in Figs. 2(d)–2(f). The pristine samples show two distinct sets of peaks, one below

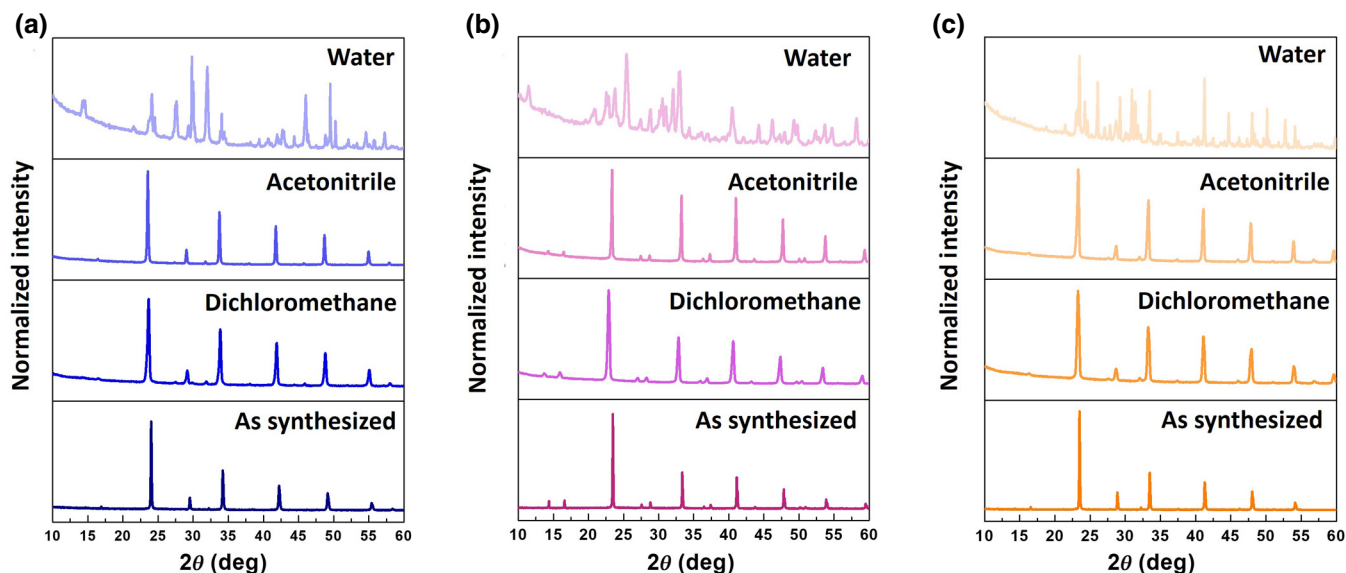


FIG. 1. X-ray diffraction patterns of (a) $\text{Cs}_2\text{AgInCl}_6$, (b) $\text{Cs}_2\text{AgBiCl}_6$, and (c) $\text{Cs}_2\text{AgSbCl}_6$ after 2 h in water, acetonitrile, and dichloromethane are compared with the as-synthesized material.

100 cm^{-1} and the other above 100 cm^{-1} . The former corresponds to bending and stretching vibrations of Ag-Cl in the $[\text{AgCl}_6]^{5-}$ octahedron, and the latter corresponds to bending and stretching modes of $M\text{-Cl}$ ($M = \text{In, Bi, Sb}$) vibrations in the $[\text{MCl}_6]^{3-}$ octahedron [36]. More details on FTIR spectra are given in our previous reports [37,38]. For CAIC [Fig. 2(d)], compared to the pristine sample (labeled *R*), broadening of the peaks is observed for In-Cl and Ag-Cl vibrations when immersed in an electrolyte (labeled *E*). This might be due to the coordination of cations with acetonitrile solvent and PF_6^- anions in supporting electrolyte. Upon oxidation (position 1), In-Cl stretching and bending vibrational modes shift to lower wave numbers and to higher wave numbers when subjected to reduction potentials.

For CABC [Fig. 2(e)], unlike CAIC, no significant change is observed between *R* and *E*, but stretching modes of Bi-Cl shift to higher wave numbers upon oxidation and to lower wave numbers upon reduction, with no change in Bi-Cl bending and Ag-Cl frequencies. For CASbC, very broad peaks are observed for Sb-Cl vibrational modes, with a slight shift to higher and lower wave numbers upon oxidation and reduction, respectively. The Ag-Cl peaks also show shifting, splitting, and broadening with no clear trend. It was shown in previous reports that an increase in the oxidation state of *M* in $[\text{MX}_6]^{n-}$ octahedra shifted the vibrational frequency to higher numbers [39–44]. In the case of CABC and CASbC, a similar trend is observed for $[\text{MCl}_6]^{3-}$ vibrations, but for CAIC the opposite trend is observed. The difference in observations between CAIC and CABC(CASbC), can be attributed to the interplay between the modification of coordination environment

happening on the surface cations of perovskites and the bond-dissociation energies ($\text{In-Cl} > \text{Sb-Cl} > \text{Bi-Cl}$) [45].

XPS data of films before and after the first CV cycle are shown in Figs. S7–S10 within the Supplemental Material [35]. One of the common observations is that the XPS signature of cesium is not affected as much as expected because its reduction potential lies far into the negative region. In CAIC, Ag and In remain similar, in spite of the observation of a strong reduction current, although some minor changes in the binding-energy positions for chloride are observed. This might be because, upon scanning to negative potentials, the degraded products dissolve or disperse in the electrolyte, leaving a fresh surface after every cycle. However, changes are observed in *M* (Bi, Sb), Ag, and Cl, indicating that surface changes do occur, with decomposed products remaining on the surface.

The salt cyclic voltammograms (Figs. S11 and S12 within the Supplemental Material [35]) of InCl_3 and SbCl_3 in DCM show the onset of reduction just below 0 V, indicating that the reduction current arises from the conversion of M^{3+} into M^0 . The SbCl_3 also shows an oxidation peak at around 0.4 V, indicating the possible oxidation of Sb^{3+} to Sb^{5+} . As AgCl and BiCl_3 are not soluble in DCM, their salt cyclic voltammograms cannot be recorded, but they are expected to reduce to their zero-valent state below 0 V. From these results, it is clear that CABC and CAIC are stable in the oxidation region between 0 and 1 V (vs Ag-AgCl), and CASbC is stable between 0 and 0.75 V (vs Ag-AgCl). Oxidation beyond 0.75 V is attributed to the oxidation of Sb^{3+} . The reduction current below 0 V in all three materials indicates the possible reduction of Ag^+ and M^{3+} (Bi, In, Sb) to Ag^0 and M^0 , respectively.

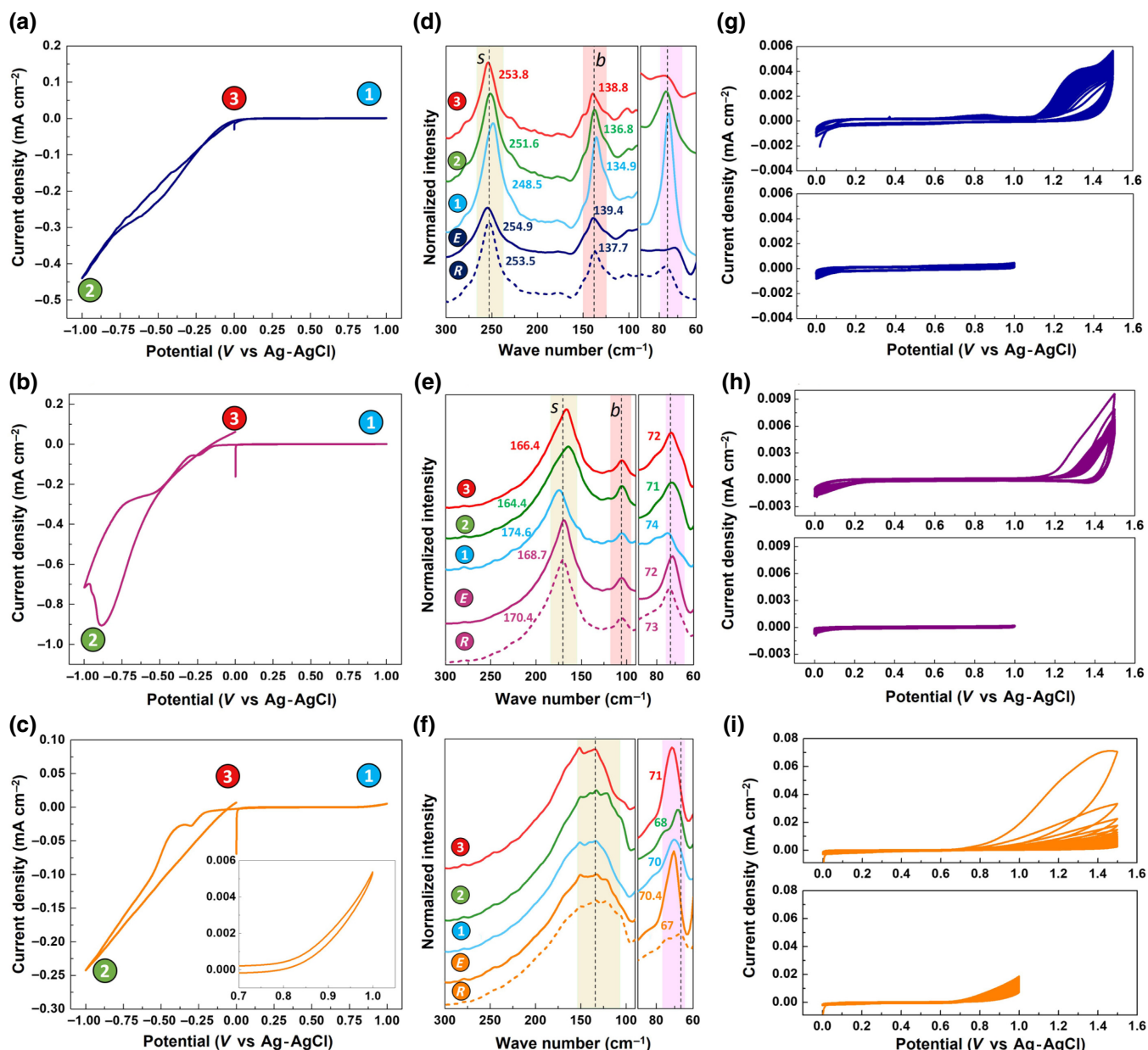


FIG. 2. (a)–(c) Cyclic voltammograms (scan rate, 5 mVs⁻¹) of CAIC, CABC, and CASbC. Numbers 1–3 represent points after oxidation (0 to 1 V), reduction (1 to –1 V), and one complete cycle, respectively. (d)–(f) Infrared spectra of CAIC, CABC, and CASbC for different samples, as mentioned for the cyclic voltammograms. *R* corresponds to the pristine sample, and *E* corresponds to a sample dipped in electrolyte. (g)–(i) One hundred cycles of CV scans (bottom panels) between 0 and 1 V and (top panels) between 0 and 1.5 V.

On the cathodic side, all three materials show irreversible reduction, leading to the decomposition of materials.

To further confirm the stability in the oxidation region, the films are cycled between (i) 0 and 1 V (vs Ag-AgCl) and (ii) 0 and 1.5 V (vs Ag-AgCl). The cyclic voltammograms are shown in Figs. 2(g)–2(i). Both CAIC and CABC show no redox signature throughout the 100 cycles between 0 and 1 V. However, upon extending the scan range, the oxidation-current onset is observed between 1.1

and 1.2 V. In CASbC, onset starts at about 0.75 V. So, the electrochemical stability window for CAIC and CABC lies between 0 V and about 1.1 V (vs Ag-AgCl), whereas for CASbC it is between 0 V and about 0.75 V (vs Ag-AgCl).

The role of scan rate, solvent (acetonitrile or DCM), and mixed trivalent compounds are also explored. The cyclic voltammograms measured at different scan rates show similar profiles, but the color of the film changes drastically at a lower scan rate, indicating significant

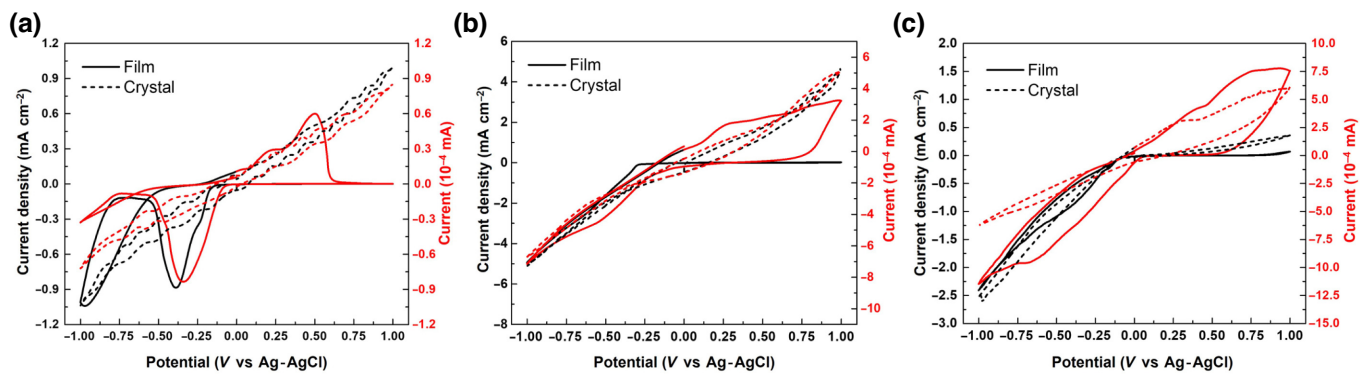


FIG. 3. Comparison of cyclic voltammograms of films (solid lines) and crystals (dotted lines) of (a) CAIC, (b) CABC, and (c) CASbC.

decomposition (Fig. S13 within the Supplemental Material [35]). When using acetonitrile instead of DCM, the current-voltage profile remains similar, and it confirms that the effect of solvent is minimal (Figs. S14–S16 within the Supplemental Material [35]). The mixed trivalent cationic materials $\text{Cs}_2\text{AgIn}_{0.5}\text{Bi}_{0.5}\text{Cl}_6$, $\text{Cs}_2\text{AgIn}_{0.5}\text{Sb}_{0.5}\text{Cl}_6$, and $\text{Cs}_2\text{AgBi}_{0.5}\text{Sb}_{0.5}\text{Cl}_6$ also show redox behavior similar to that of their parent materials (Figs. S17–S19 within the Supplemental Material [35]). Finally, to understand the origin (bulk or surface) of the redox peaks, the electrochemistry of the polycrystalline films is compared to that of single crystals. Sufficiently large crystals are grown, and single-crystal electrochemistry is carried out. Figure 3 shows the cyclic voltammograms of single crystals and polycrystalline films. CAIC and CABC show almost linear currents for both oxidation and reduction potentials, and a similar linear current is observed for CASbC crystals, but the slopes of the oxidation and reduction sides are different. There are no distinct redox peaks in the crystals, unlike the observations in films. It can be hypothesized that the redox peaks in the polycrystalline films arise from surface cationic sites, whereas in the single crystals, as the surface area is low, no such observation is made. The bulk of the material encounters no redox process.

As these materials are stable in the oxidation region, they can be exploited to carry out PEC oxidation reactions, such as oxygen-evolution reactions (OERs). Since these materials are not stable in water, a mixture of ACN and water is employed. At a ratio of 1:9 water to acetonitrile, all three materials remain stable, as confirmed by the XRD patterns, as shown in Figs. 4(a)–4(c).

To identify the band positions, Mott-Schottky (M-S) studies are carried out in a mixture of acetonitrile and water (90:10) solvent with TBAPF₆ as a supporting electrolyte. Figure 4(d) shows the M-S plot derived from an electrochemical impedance spectrum measured at a frequency of 920 Hz. The flat-band potentials (V_{FB}) are found to be -0.25 , -0.33 , and -0.15 V (vs Ag-AgCl) for CAIC, CABC and CASbC, respectively. V_{FB} measured at other

frequencies of 514, 287, and 109 Hz also has similar values (Fig. S20 within the Supplemental Material [35]). The positive slopes of the M-S plots indicate that all the double perovskite materials under study are *n* type in nature. From the optical band gap (Fig. S21 within the Supplemental Material [35]) and flat-band potentials, the band positions are derived, as shown in Fig. 4(e). All three materials possess valence bands lower than the water-oxidation potential. The oxidative stability, *n*-type behavior, and appropriate valence-band alignment make these materials suitable photoanodes for PEC water oxidation.

The photoelectrochemical water oxidation is carried out in acetonitrile and water (90:10 vol.-vol.) with CAIC, CABC and CASbC as absorbers and TBAPF₆ as the supporting electrolyte. The absorbers are coated on cleaned fluorine-doped tin oxide (FTO) with a thin TiO₂ underlayer deposited by the TiCl₄ chemical bath deposition technique. Platinum coil and Ag-AgCl are used as counter and reference electrodes, respectively. The pH value for the mixture of acetonitrile and water is measured to be around 7–7.2. Figure 5(a) shows PEC water oxidation under dark and AM1.5G illumination conditions. The blank LSV measurement without perovskite absorber layers but with an underlayer of titanium dioxide shows a very low photocurrent of $7 \mu\text{A cm}^{-2}$ at 0.61 V (vs Ag-AgCl, equivalent to 1.23 V vs RHE, Fig. S22 within the Supplemental Material [35]). The photoanode with CAIC shows a photocurrent density of 0.29 mA cm^{-2} at 0.61 V. CABC shows a slightly higher current density of 0.34 mA cm^{-2} . CASbC, on the other hand, shows the lowest current density among these three absorbers. To verify that the photocurrent arises from water oxidation, chopped-light measurements are carried out. For CAIC and CABC, the chopped-light data match with the LSVs of continuous light and dark measurements, ruling out photocorrosion, whereas, for CASbC, at voltages between 0 and about 0.6 V, the chopped-illumination current is lower than the continuous-illumination current. Although under dark conditions, it was previously shown that the material remained stable between 0 and

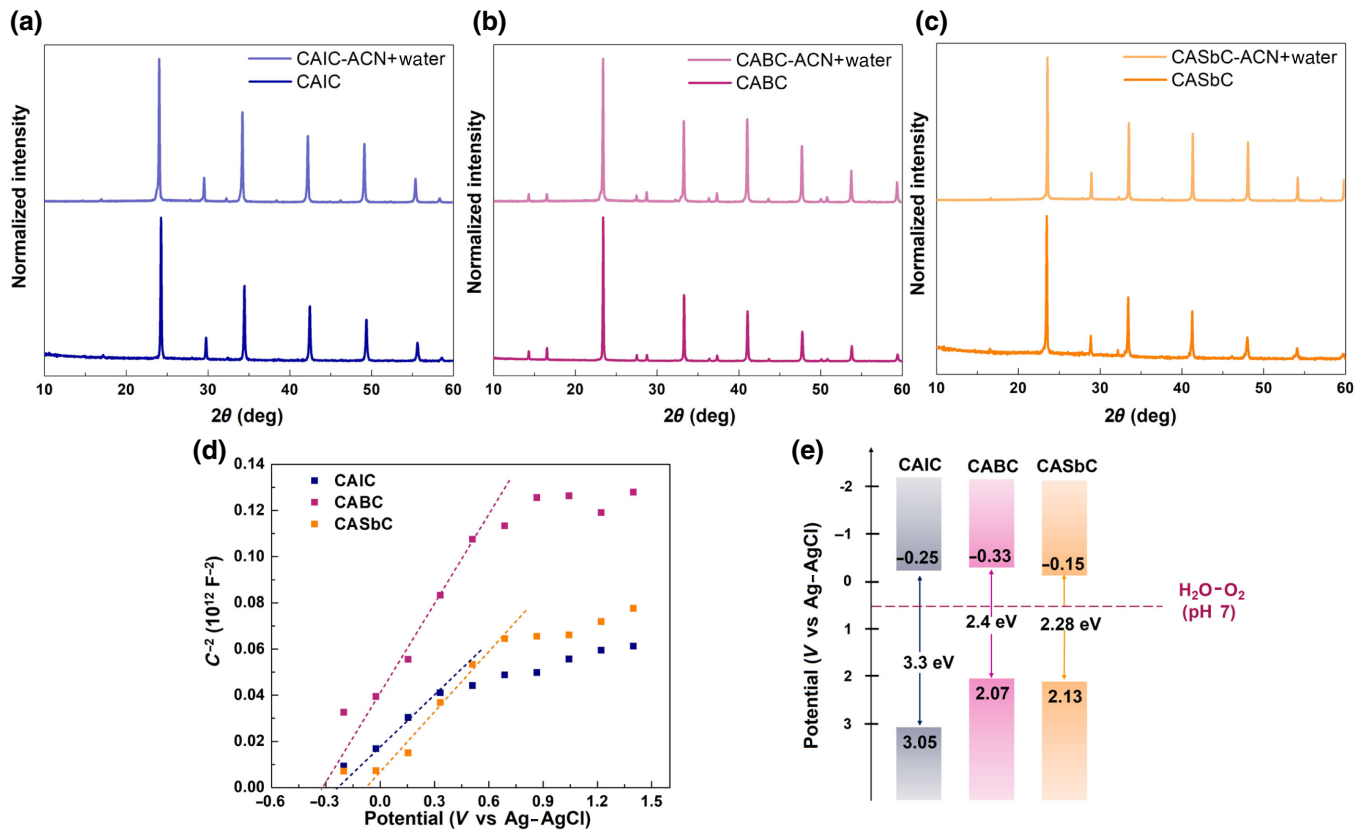


FIG. 4. Powder XRD patterns of (a) CAIC, (b) CABC, and (c) CASbC in ACN + DI water (90:10) dipped for 2 h are compared with the as-synthesized samples. (d) Mott-Schottky plot showing the flat-band potential, and (e) band positions of samples derived from the Mott-Schottky plot; absorption spectra are shown in Figs. S20 and S21 within the Supplemental Material [35].

0.8 V; under illumination, the difference in current density between chopped-light and continuous illumination indicates the possibility of photocorrosion. The onset potentials for water oxidation for all three materials are observed at approximately 0.1 V (vs Ag-AgCl).

To enhance the catalytic activity for water oxidation, these films are separately coated with IrO_x , which is a well-known OER catalyst. The IrO_x cocatalyst on CAIC improves the photocurrent density to 0.5 mA cm^{-2} (at 0.61 V vs Ag-AgCl), and for CABC, the corresponding value increases to 0.43 mA cm^{-2} . Unlike these two materials, CASbC shows a lower performance in the presence of a cocatalyst. The chopped-light measurements show no photocorrosion in CAIC and CABC with the IrO_x cocatalyst, but CASbC shows some photocorrosion at lower voltages. Overall, the PEC activity is shown to be highest for CAIC with IrO_x . It has to be noted that CAIC has a wide band gap of 3.3 eV, which absorbs only the UV region of the solar spectrum. Theoretically, CAIC can generate a photocurrent density of 0.82 mA cm^{-2} if all the photons with $E \geq 3.3 \text{ eV}$ are absorbed. Bare CAIC with a photocurrent density of 0.29 mA cm^{-2} indicates that more than 34% of the incident photons are converted into current. With the IrO_x cocatalyst, this conversion drastically increases to

60%. With just 400–600-mV overpotential (~ 1.01 – 1.21 V vs Ag-AgCl), the photocurrent density of CAIC with the IrO_x cocatalyst increases to over 0.75 mA cm^{-2} , and it corresponds to 80–88% conversion. The PEC device with CABC converts nearly 4.5–5.7% of incident photons into current. Whereas, for CASbC, it lies between 1.2 and 1.6%. Among these three materials, $I_{\text{experimental}}/I_{\text{theoretical}}$ for CAIC is at least 12 times more than CABC, and nearly 38 times that of CASbC for PEC water oxidation.

To confirm the reproducibility of CAIC, multiple LSV measurements are carried out with different photoanodes and an average LSV with error bars is given in Fig. 5(d). The chronoamperometry results in Fig. 5(e) show that the photocurrent density remains stable over a period of 600 s. These results indicate the reproducibility and stability of CAIC under photoelectrochemical water-oxidation conditions. Oxygen evolution for the best-performing IrO_x -coated $\text{Cs}_2\text{AgInCl}_6$ is studied using gas chromatography. The experiment is carried out in a two-necked gas-tight round-bottomed flask with an acetonitrile-water mixture as the electrolyte, platinum as the counter electrode, Ag-AgCl as the reference electrode, and IrO_x -coated $\text{Cs}_2\text{AgInCl}_6$ as the working electrode, with an applied potential of 0.6 V (vs Ag-AgCl) for 2 h. During the first 30 min, the device

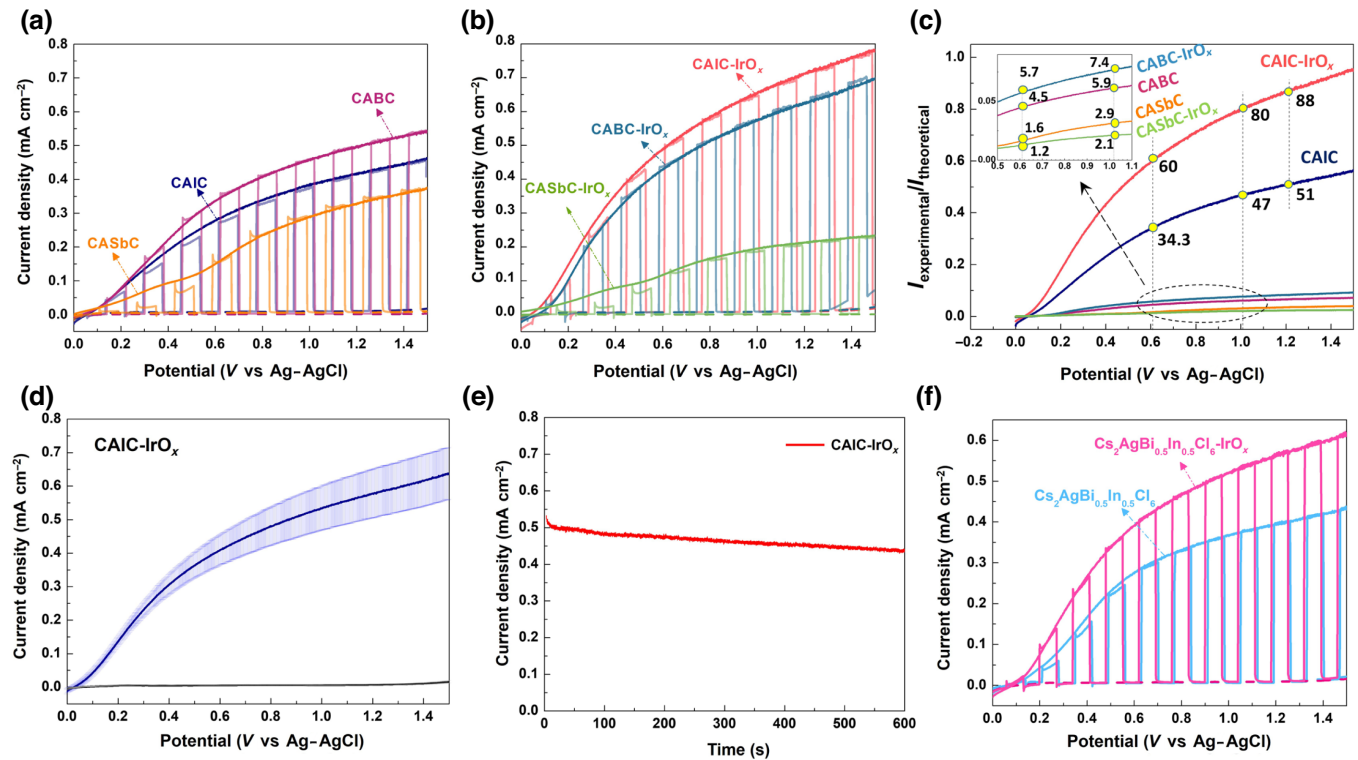


FIG. 5. Linear-sweep voltammograms (LSV) of (a) bare and (b) IrO_x -coated CAIC, CABC, and CASbC photoanodes under dark (dotted line) and continuous and chopped AM1.5G illumination (solid lines). (c) Ratio of experimentally observed current density ($I_{\text{experimental}}$) to the theoretical maximum current density ($I_{\text{theoretical}}$) as a function of applied potential. $I_{\text{experimental}}$ is obtained from the LSVs shown in (a),(b), and $I_{\text{theoretical}}$ is obtained from the AM1.5G spectra for a given band gap of the material. Dashed vertical line at 0.61 V (vs Ag-AgCl) is equivalent to 1.23 V (vs RHE), and the dashed lines at 1.01 and 1.21 V correspond to 400- and 600-mV overpotential for water oxidation, respectively. (d) LSV shows the repeatability of performance of at least three IrO_x -coated CAIC samples. Average value with the error bar is shown. (e) Photocurrent density as a function of time for IrO_x -coated CAIC under illumination, at 0.61 V (vs Ag-AgCl). (f) LSVs of $\text{Cs}_2\text{AgBi}_{0.5}\text{In}_{0.5}\text{Cl}_6$ with and without IrO_x cocatalyst.

is kept in the dark. This step is done to observe any baseline oxygen production under dark conditions. After 30 min, the device is illuminated with an AM1.5G solar simulator (100-mW cm^{-2} optical flux) and illumination is maintained for 90 min. Gas sampling is done, from the head space of the reactor, every 30 min, and samples are analyzed using a gas chromatograph fitted with a thermal conductivity detector. Oxygen calibration is done using precalibrated gas bottles. Figure S23 within the Supplemental Material [35] shows the oxygen concentration in the head space. It is observed that no oxygen is generated in the dark for the first 30 min, even with an applied potential. However, under illumination, oxygen is generated up to $500\ \mu\text{mol}$. The generation of oxygen is linear as a function of time, indicating the stable water-oxidation capability of the halide double perovskite absorber. To understand the stability of these materials after photoelectrochemical water-oxidation reactions, we record the powder XRD patterns of the materials after the reaction (Fig. S24 within the Supplemental Material [35]). Powder XRD data show patterns similar to that of the parent material, with minor

impurity peaks corresponding to AgCl or InCl_3 . Although there is minor phase disintegration of $\text{Cs}_2\text{AgInCl}_6$ to AgCl and InCl_3 , which is only possible at the surface, the water-oxidation capability remains constant without any drop in performance. In the case of bismuth- and antimony-based compounds, only AgCl impurities appear, but no indication of trivalent salts is observed.

In one of our previous reports, we showed that the photoluminescence excited-state lifetimes of CAIC and CABC were in the order of a few hundreds of picoseconds; however, the mixed trivalent cationic sites in $\text{Cs}_2\text{AgIn}_x\text{Bi}_{1-x}\text{Cl}_6$ increased the value to several hundreds of nanoseconds due to the presence of local polarization. In general, the excited-state lifetime is related to the recombination rate, and since the mixed trivalent cation has a longer lifetime, we investigate the PEC activity of $\text{Cs}_2\text{AgIn}_{0.5}\text{Bi}_{0.5}\text{Cl}_6$ with and without IrO_x [Fig. 5(f)]. The observed photocurrent density, however, is lower compared to that of the parent compounds. This might be attributed to the sluggish transport rate due to the localization of photogenerated excitons at the polarized sites [38].

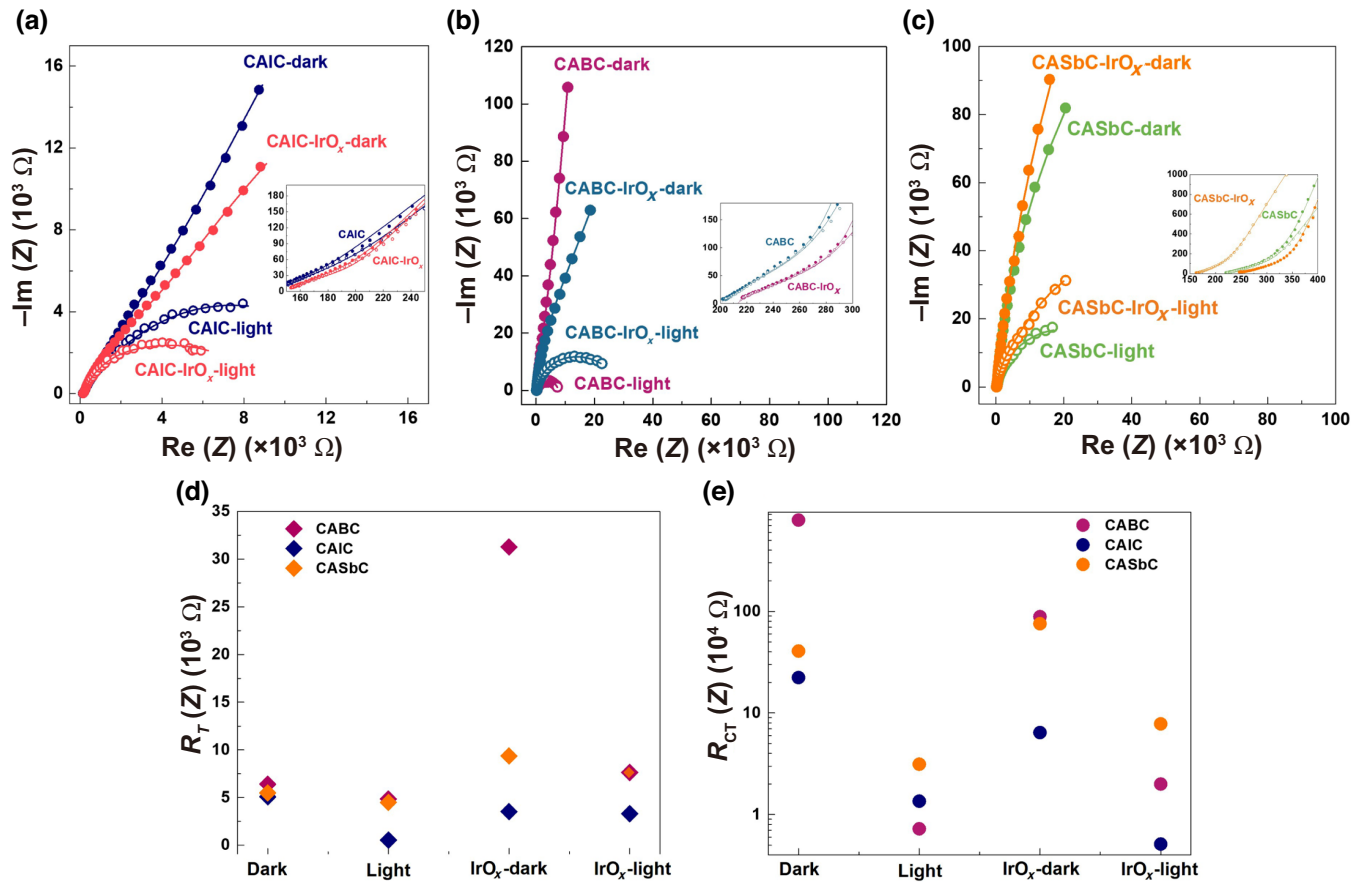


FIG. 6. Nyquist electrochemical impedance plots of PEC devices with (a) CAIC, (b) CABC, and (c) CASbC absorbers, with and without IrO_x coating, recorded at 0.61 V. Inset represents magnified values at higher frequencies. (d) Plot of transport resistance of carriers in perovskite absorbers with and without IrO_x to show that the resistance under light is small compared to dark. (e) Plot of charge-transfer resistance in the dark and light. Charge-transfer resistance under light is very small compared to the dark resistance.

It is also possible that the surface catalytic activity might be affected due to the presence of mixed trivalent sites. Further investigation is required to understand the latter class of mixed trivalent materials.

To understand the PEC water-oxidation properties of CAIC, CABC, and CASbC, it is essential to investigate the properties of light absorption, rate of charge transport and recombination, and the efficiency of charge transfer from the valence band of the absorber to the electrolyte or cocatalyst. To understand the transport and recombination rates, electrochemical impedance spectroscopy (EIS) measurements are carried out on PEC devices at 0.6 V (vs Ag-AgCl) under light and dark conditions (Fig. 6). The EIS spectra are fitted with an equivalent circuit containing a resistor and three constant-phase resistor elements connected in series, where R_1 , R_2 , R_T , and R_{CT} correspond to the contact resistance, the resistance at the TiO₂ layer, transport resistance in the bulk of the absorber, and the resistance to charge transfer to the electrolyte, respectively. The values of R_1 and R_2 remain the same in the light and dark, whereas R_T and R_{CT} values decrease under

illumination. The R_T values under light are found to be low for CAIC (538 Ω), and they are almost the same for CABC (4838 Ω) and CASbC (4484 Ω). On the other hand, R_{CT} values are lower in CABC (7252 Ω), followed by CAIC (13 553 Ω) and CASbC (31 325 Ω). Although CAIC has a low transport resistance, charge transfer (R_{CT}) determines the performance of PEC water oxidation. The trend of R_{CT} , that is, the resistance to charge transfer from the valence band of the absorber to the electrolyte, is in line with observations of the photocurrent density shown in Fig. 5(a). EIS measurements are carried on PEC devices with an IrO_x cocatalyst, and these data are also fitted with the same equivalent circuit. R_1 and R_2 remain unaffected by light, and the trend observed for R_T is similar to that of the previous case. However, the value of R_{CT} decreases drastically for CAIC-IrO_x (5132 Ω) compared to CAIC (13 553 Ω). For the other two compounds, the R_{CT} values increase in the presence of the IrO_x coating. These results indicate that charge transfer from the valence band of the photoanode to the cocatalyst (and eventually to the electrolyte) is enhanced for CAIC and decreases for

CABC and CASbC. In our previous report, we showed that the excited-state lifetime of electrons was longer for CAIC compared to CABC, indicating low bulk carrier recombination for the former [38]. The combination of low recombination, higher charge transport, and enhanced hole injection to the electrolyte with the CAIC- IrO_x photoanode leads to a high photooxidation current density of 0.5 mA cm^{-2} at 1.23 V versus RHE. An overpotential of 400 mV leads to a very high value of 0.75 mA cm^{-2} with over 80% absorbed photon-to-current conversion. CABC and CASbC have similar absorption onset and transport resistances, but R_{CT} is higher for the latter, leading to an inferior PEC performance of CASbC.

III. CONCLUSION

Here, the electrochemical properties and, subsequently, photoelectrochemical water oxidation are investigated in stable halide double perovskite materials, $\text{Cs}_2\text{AgMCl}_6$ ($M = \text{Bi, In, Sb}$). $\text{Cs}_2\text{AgInCl}_6$ and $\text{Cs}_2\text{AgBiCl}_6$ show extraordinary oxidative stability between 0 and 1.1 V (vs Ag-AgCl), whereas $\text{Cs}_2\text{AgSbCl}_6$ remains stable between 0 and 0.75 V (vs Ag-AgCl). However, all three materials show a steep reduction below 0 V (vs Ag-AgCl). With the combination of FT-far-IR and XPS studies, we conclude that Ag^+ and M^{3+} cations reduce to a possible metallic state, leading to perovskite decomposition. The electrochemistry of single crystals and polycrystalline films reveals that these reduction reactions happen predominantly on the surface. The effects of scan rate and solvents on the electrochemical properties are also investigated. The oxidative stability of materials, coupled with appropriate band positions and the n -type nature of conductivity, enable us to employ these materials in solar photoelectrochemical water oxidation in a near-neutral electrolyte containing 90:10 (vol.-vol.) $\text{CH}_3\text{CN} : \text{H}_2\text{O}$ solvent, with and without IrO_x cocatalyst. At the thermodynamic water-oxidation potential of 1.23 V versus RHE, the $\text{Cs}_2\text{AgInCl}_6$ photoabsorbers show a current of 0.5 mA cm^{-2} and at an applied overpotential of 400–600 mV the current increases to over 0.75 mA cm^{-2} . Based on the band gap, CAIC should theoretically have a value of around 0.82 mA cm^{-2} . Experimentally, we obtain more than 60% of the theoretical maximum current at 1.23 V versus RHE, and at 600-mV overpotential the value is nearly 90%. This PEC device also shows excellent stability and reproducibility. The fundamental charge-transfer process is investigated by EIS, where both the rate of carrier transport and recombination are found to influence the device performance. Unlike the conventional ABX_3 perovskite, these double perovskite materials show stability for over 1 year under our laboratory conditions (Fig. S25 within the Supplemental Material [35]). The stability coupled with extraordinary PEC water-oxidation capability make these materials suitable for next-generation solar water-splitting devices.

IV. EXPERIMENTAL SECTION

A. Materials

Cesium chloride (CsCl , 99.99%), silver chloride (AgCl , 99.99%), indium chloride (InCl_3 , 99.99%), bismuth chloride (BiCl_3 , 99.99%), and antimony chloride (SbCl_3 , 99.99%) are purchased from Alfa Aesar. Hydrochloric acid (HCl , 37.8%) and isopropyl alcohol ($\text{C}_3\text{H}_8\text{O}$) are purchased from the Rankem company. Tris(2,4-pentanedionato)iridium(III) [iridium acetyl acetonate, $\text{Ir}(\text{acac})_3$] is purchased from TCI India. TBAPF₆ (98%) and DCM (anhydrous, >99.8%) are purchased from Sigma-Aldrich. Chloroform (CHCl_3 , 98%) and HPLC-grade acetonitrile (CH_3CN , 99.8%) are procured from ThermoFisher Scientific. Epoxy is purchased from local stores. FTO glass (TEC7) is procured from Dyesol, Australia.

B. Synthesis of $\text{Cs}_2\text{AgMCl}_6$ ($M = \text{In, Bi, Sb}$)

2 mmol of CsCl ; 1 mmol of AgCl ; and 1 mmol of InCl_3 , BiCl_3 , or SbCl_3 are added to 10 M of hydrochloric acid, ultrasonicated for 60 min, and the sonicated mixture is transferred to a stainless-steel autoclave reactor (hydrothermal reactor) and kept in a hot-air oven at 180 °C for 12 h (where the time taken to reach 180 °C is set to 45 min). The hydrothermal reactor is then allowed to cool to room temperature before opening, to avoid any sudden release of pressure. The obtained powdered material is then filtered, washed with $\text{C}_3\text{H}_8\text{O}$, and dried at 70 °C before use. The synthesis of materials with mixed trivalent cations, $\text{Cs}_2\text{AgBi}_{0.5}\text{In}_{0.5}\text{Cl}_6$, $\text{Cs}_2\text{AgBi}_{0.5}\text{Sb}_{0.5}\text{Cl}_6$, and $\text{Cs}_2\text{AgIn}_{0.5}\text{Sb}_{0.5}\text{Cl}_6$, is done by using appropriate mole fractions of salts of the trivalent cations.

For the synthesis of single crystals, the above procedure is followed, but the reactor is cooled slowly from 180 to 60 °C over a period of 72 h for $\text{Cs}_2\text{AgInCl}_6$ and $\text{Cs}_2\text{AgSbCl}_6$ and 48 h for $\text{Cs}_2\text{AgBiCl}_6$.

C. Stability test

A known amount of $\text{Cs}_{2\text{Ag}}\text{MCl}_6$ ($M = \text{In}^{3+}, \text{Bi}^{3+}, \text{Sb}^{3+}$) is transferred to a petri dish and then dispersed in water, DCM, and ACN individually, and kept for 2 h. In the case of water, an immediate change of color is observed, indicating material degradation, whereas for nonaqueous solvents, i.e., DCM and ACN, no such changes are observed, showing stability. Powder XRD analysis is done for these materials after drying.

D. Electrophoretic deposition

FTO glass is cut into $2 \times 1.5 \text{ cm}^2$ pieces; ultrasonically cleaned with $\text{C}_3\text{H}_8\text{O}$, dilute HCl , and $\text{C}_3\text{H}_8\text{O}$, for 20 min each; heated on a hot plate at 500 °C for 1 h; and cooled to room temperature. The as-prepared powdered material is finely ground using a mortar and pestle. Then, 150 mg of

the finely ground material is dispersed in 50 ml of ethanol and sonicated for a few minutes before electrophoretic deposition. Two small cleaned FTO glass pieces (one acting as the working electrode and the other as a counter electrode) are taken, connected to a dc power supply (Delta Electronika, ES0300-0.45), and dipped into the dispersed solution with the conducting sides facing each other. A potential of 50 V is applied between these two FTO glass pieces for 7 min to obtain a uniform film on the FTO substrate. Deposition happens at the positive electrode.

The electrophoretic deposition of $\text{Cs}_2\text{AgSbCl}_6$ results in the degradation of this material. So, $\text{Cs}_2\text{AgSbCl}_6$ films are prepared by spin coating the dispersed ethanolic solution of $\text{Cs}_2\text{AgSbCl}_6$ on the FTO substrate at 50–100 rpm for 1 min. Spin coating is repeated multiple times to obtain a uniform and thin film. The deposited films are then dried at 70 °C overnight to make them more compact.

E. Characterization methods

Absorption spectra are recorded using a Shimadzu UV-2600 UV-Vis-NIR absorption spectrophotometer fitted with a BaSO_4 -coated integrating sphere. X-ray diffraction patterns are collected using a D8 Advance Bruker instrument with a $\text{CuK}\alpha$ source. Electrochemical studies are carried out in a three-electrode cell using an SP-300 Biologic electrochemical workstation. The electrophoretically deposited and spin-coated films of $\text{Cs}_2\text{AgMCl}_6$ on FTO function as the working electrode, Ag-AgCl (sat.) electrode as the reference electrode, and platinum (Pt) coil as a counter electrode (cleaned using dilute nitric acid solution, water, and finally DCM). The working electrodes for single-crystal electrochemical studies are prepared as shown in Fig. S26 within the Supplemental Material [35], where the single crystals of $\text{Cs}_2\text{AgMCl}_6$ are connected to a conducting glass substrate using conducting silver paste and then dried at 70 °C for a few minutes. Furthermore, the area around the crystals that comes into contact with the electrolyte is covered using insulating epoxy.

The FTIR spectra for electrophoretic films are obtained using an ATR-fitted JASCO 6600FV spectrometer. The spectrometer is operated under complete vacuum for far-IR measurements. The x-ray photoelectron spectroscopy (XPS) measurements are done using a PHI Versaprobe III instrument using an $\text{AlK}\alpha$ source (1486.6 eV). Data are fitted using CASA XPS software, and all spectra are calibrated using the C 1s peak at 284.6 eV.

F. Photoelectrochemical characterization

Cleaned FTO glass is coated with two thin TiO_2 blockings underlayers, one by spray pyrolysis and the other by chemical bath deposition. Spray pyrolysis is done on cleaned FTO glass heated to 450 °C by spraying a mixture of 1-ml titanium di(isopropoxide) bis(acetylacetonate) and 39-ml ethanol, followed by pyrolysis for 5 min at

the same temperature. The second layer is coated using a chemical bath containing 300-mM TiCl_4 . After placing the substrates in the TiCl_4 solution, they are heated to 75 °C for 30 min. $\text{Cs}_2\text{AgMCl}_6$ films are deposited on TiO_2 -coated FTO, using the abovementioned electrophoretic and spin-coating methods. The electrolyte used is 10:90 deionized water and acetonitrile containing 0.01-M TBAPF₆ as the supporting electrolyte. A piece of film ($0.5 \times 0.5 \text{ cm}^2$) is retained after scrapping the remaining portion of material on FTO. PEC measurements are carried out in a homemade cappuccino cell under dark and simulated AM1.5G sunlight using a ScienceTech (Canada) solar simulator. The working electrode is $\text{Cs}_2\text{AgMCl}_6/\text{TiO}_2$ -coated FTO with and without a cocatalyst layer. Ag-AgCl (sat. KCl) and Pt coil are used as the reference electrode and counter electrode, respectively. Chopped-light measurements are carried out using a homemade optical chopper with an Arduino microcontroller board, with an *on-off* interval time of 10 s. Constant-voltage measurements are carried out using an SP-300 Biologic electrochemical workstation.

G. IrO_x deposition

A 0.1 M solution of iridium acetylacetonate in chloroform is spin coated at 3000 rpm for 60 s. After coating, the substrate is heated at 100 °C for 1 h and treated with a 2-W AstraSpot blue light-emitting diode (420 nm) (Philips model no. 58914) for 10 min.

H. Electrochemical impedance studies

Electrochemical impedance studies for CAIC, CABC, and CASbC are carried out using the three-electrode PEC setup, where an ac amplitude of 15 mV is superimposed with a dc potential of 0.6 V (vs Ag-AgCl) in the frequency range of 1 MHz to 100 mHz, under both dark and AM1.5G light. Mott-Schottky analysis is done by plotting $1/C^2$ versus V , where C is the capacitance calculated from the formula $Z_{\text{im}} = 1/\omega C$, in which ω is frequency taken as 920.3, 513.85, 286.93, and 108.7 Hz, and Z_{im} is taken from EIS data.

ACKNOWLEDGMENTS

This project is funded by Nanomission, Department of Science and Technology, Government of India, under Grant No. DST/NM/NT/2018/82.

-
- [1] M. A. Modestino and S. Haussener, An integrated device view on photo-electrochemical solar-hydrogen generation, *Annu. Rev. Chem. Biomol. Eng.* **6**, 13 (2015).
 [2] Y. Tachibana, L. Vayssieres, and J. R. Durrant, Artificial photosynthesis for solar water-splitting, *Nat. Photonics* **6**, 511 (2012).

- [3] M. Saliba, T. Matsui, J. Y. Seo, K. Domanski, J. P. Correa-Baena, M. K. Nazeeruddin, S. M. Zakeeruddin, W. Tress, A. Abate, A. Hagfeldt, and M. Grätzel, Cesium-containing triple cation perovskite solar cells: Improved stability, reproducibility and high efficiency, *Energy Environ. Sci.* **9**, 1989 (2016).
- [4] Z. Tang, T. Bessho, F. Awai, T. Kinoshita, M. M. Maitani, R. Jono, T. N. Murakami, H. Wang, T. Kubo, S. Uchida, and H. Segawa, Hysteresis-free perovskite solar cells made of potassium-doped organometal halide perovskite, *Sci. Rep.* **7**, 1 (2017).
- [5] W. S. Yang, B. W. Park, E. H. Jung, N. J. Jeon, Y. C. Kim, D. U. Lee, S. S. Shin, J. Seo, E. K. Kim, J. H. Noh, and S. Il Seok, Iodide management in formamidinium-lead-halide-based perovskite layers for efficient solar cells, *Science* **356**, 1376 (2017).
- [6] J. Y. Kim, J. W. Lee, H. S. Jung, H. Shin, and N. G. Park, High-efficiency perovskite solar cells, *Chem. Rev.* **120**, 7867 (2020).
- [7] J. Jeong, *et al.*, Pseudo-halide anion engineering for α -FAPbI₃ perovskite solar cells, *Nature* **592**, 381 (2021).
- [8] G. Grancini and M. K. Nazeeruddin, Dimensional tailoring of hybrid perovskites for photovoltaics, *Nat. Rev. Mater.* **4**, 4 (2019).
- [9] H.-S. Kim, J.-Y. Seo, and N.-G. Park, Material and device stability in perovskite solar cells, *ChemSusChem* **9**, 2528 (2016).
- [10] H. S. Jung and N.-G. Park, Perovskite solar cells: From materials to devices, *Small* **11**, 10 (2015).
- [11] T. A. Berhe, W. N. Su, C. H. Chen, C. J. Pan, J. H. Cheng, H. M. Chen, M. C. Tsai, L. Y. Chen, A. A. Dubale, and B. J. Hwang, Organometal halide perovskite solar cells: Degradation and stability, *Energy Environ. Sci.* **9**, 323 (2016).
- [12] N. Aristidou, I. Sanchez-Molina, T. Chotchuangchutchaval, M. Brown, L. Martinez, T. Rath, and S. A. Haque, The role of oxygen in the degradation of methylammonium lead trihalide perovskite photoactive layers, *Angew. Chem., Int. Ed.* **54**, 8208 (2015).
- [13] S. Pont, D. Bryant, C. T. Lin, N. Aristidou, S. Wheeler, X. Ma, R. Godin, S. A. Haque, and J. R. Durrant, Tuning CH₃NH₃Pb(I_{1-x}Br_x)₃ perovskite oxygen stability in thin films and solar cells, *J. Mater. Chem. A* **5**, 9553 (2017).
- [14] H. S. Rao, B. X. Chen, X. D. Wang, D. Bin Kuang, and C. Y. Su, A micron-scale laminar MAPbBr₃ single crystal for an efficient and stable perovskite solar cell, *Chem. Commun.* **53**, 5163 (2017).
- [15] K. Kwak, E. Lim, N. Ahn, J. Heo, K. Bang, S. K. Kim, and M. Choi, An atomistic mechanism for the degradation of perovskite solar cells by trapped charge, *Nanoscale* **11**, 11369 (2019).
- [16] Y. Ouyang, Y. Li, P. Zhu, Q. Li, Y. Gao, J. Tong, L. Shi, Q. Zhou, C. Ling, Q. Chen, Z. Deng, H. Tan, W. Deng, and J. Wang, Photo-oxidative degradation of methylammonium lead iodide perovskite: Mechanism and protection, *J. Mater. Chem. A* **7**, 2275 (2019).
- [17] P. Da, M. Cha, L. Sun, Y. Wu, Z. S. Wang, and G. Zheng, High-performance perovskite photoanode enabled by Ni passivation and catalysis, *Nano Lett.* **15**, 3452 (2015).
- [18] S. Nam, C. T. K. Mai, and I. Oh, Ultrastable photoelectrodes for solar water splitting based on organic metal halide perovskite fabricated by lift-off process, *ACS Appl. Mater. Interfaces* **10**, 14659 (2018).
- [19] C. Wang, S. Yang, X. Chen, T. Wen, and H. G. Yang, Surface-functionalized perovskite films for stable photoelectrochemical water splitting, *J. Mater. Chem. A* **5**, 910 (2017).
- [20] R. Tao, Z. Sun, F. Li, W. Fang, and L. Xu, Achieving organic metal halide perovskite into a conventional photoelectrode: Outstanding stability in aqueous solution and high-efficient photoelectrochemical water splitting, *ACS Appl. Energy Mater.* **2**, 1969 (2019).
- [21] I. Poli, U. Hintermair, M. Regue, S. Kumar, E. V. Sackville, J. Baker, T. M. Watson, S. Eslava, and P. J. Cameron, Graphite-protected CsPbBr₃ perovskite photoanodes functionalised with water oxidation catalyst for oxygen evolution in water, *Nat. Commun.* **10**, 1 (2019).
- [22] H. Choi, S. Seo, J. H. Kim, J. H. Lee, S. Kim, G. Piao, H. Park, K. Lee, and S. Lee, An organometal halide perovskite photocathode integrated with a MoS₂ catalyst for efficient and stable photoelectrochemical water splitting, *J. Mater. Chem. A* **9**, 22291 (2021).
- [23] S. Pan, J. Li, Z. Wen, R. Lu, Q. Zhang, H. Jin, L. Zhang, Y. Chen, and S. Wang, Halide perovskite materials for photo(electro)chemical applications: Dimensionality, heterojunction, and performance, *Adv. Energy Mater.* **12**, 2004002 (2021).
- [24] M. Crespo-Quesada, L. M. Pazos-Outón, J. Warnan, M. F. Kuehnel, R. H. Friend, and E. Reisner, Metal-encapsulated organolead halide perovskite photocathode for solar-driven hydrogen evolution in water, *Nat. Commun.* **7**, 6 (2016).
- [25] S. Ahmad, A. Sadhanala, R. L. Z. Hoye, V. Andrei, M. H. Modarres, B. Zhao, J. Rongé, R. Friend, and M. De Volder, Triple-cation-based perovskite photocathodes with AZO protective layer for hydrogen production applications, *ACS Appl. Mater. Interfaces* **11**, 23198 (2019).
- [26] L. F. Gao, W. J. Luo, Y. F. Yao, and Z. G. Zou, An all-inorganic lead halide perovskite-based photocathode for stable water reduction, *Chem. Commun.* **54**, 11459 (2018).
- [27] H. Zhang, Z. Yang, W. Yu, H. Wang, W. Ma, X. Zong, and C. Li, A sandwich-like organolead halide perovskite photocathode for efficient and durable photoelectrochemical hydrogen evolution in water, *Adv. Energy Mater.* **8**, 1800795 (2018).
- [28] I. S. Kim, M. J. Pellin, and A. B. F. Martinson, Acid-compatible halide perovskite photocathodes utilizing atomic layer deposited TiO₂ for solar-driven hydrogen evolution, *ACS Energy Lett.* **4**, 293 (2019).
- [29] M. Hamdan and A. K. Chandiran, Cs₂PtI₆ halide perovskite is stable to air, moisture, and extreme pH: Application to photoelectrochemical solar water oxidation, *Angew. Chem., Int. Ed.* **59**, 16033 (2020).
- [30] X. Yang, W. Wang, R. Ran, W. Zhou, and Z. Shao, Recent advances in Cs₂AgBiBr₆-based halide double perovskites as lead-free and inorganic light absorbers for perovskite solar cells, *Energy Fuels* **34**, 10513 (2020).
- [31] E. Greul, M. L. Petrus, A. Binek, P. Docampo, and T. Bein, Highly stable, phase pure Cs₂AgBiBr₆ double perovskite

- thin films for optoelectronic applications, *J. Mater. Chem. A* **5**, 19972 (2017).
- [32] T. Wang, D. Yue, X. Li, and Y. Zhao, Lead-free double perovskite $\text{Cs}_2\text{AgBiBr}_6/\text{RGO}$ composite for efficient visible light photocatalytic H_2 evolution, *Appl. Catal., B* **268**, 118399 (2020).
- [33] M. Shi, G. Li, W. Tian, S. Jin, X. Tao, Y. Jiang, E. A. Pidko, R. Li, and C. Li, Understanding the effect of crystalline structural transformation for lead-free inorganic halide perovskites, *Adv. Mater.* **32**, 2002137 (2020).
- [34] Y. Wang, H. Huang, Z. Zhang, C. Wang, Y. Yang, Q. Li, and D. Xu, Lead-free perovskite $\text{Cs}_2\text{AgBiBr}_6@g\text{-C}_3\text{N}_4$ Z-scheme system for improving CH_4 production in photocatalytic CO_2 reduction, *Appl. Catal., B* **282**, 119570 (2021).
- [35] See the Supplemental Material at <http://link.aps.org/supplemental/10.1103/PhysRevApplied.19.044083> for additional material, including structural, optical, and electrochemical characterization data.
- [36] W. M. A. Smit, G. J. Dirksen, and D. J. Stufkens, Infrared and Raman spectra of the elpasolites $\text{Cs}_2\text{NaSbCl}_6$ and $\text{Cs}_2\text{NaBiCl}_6$: Evidence for a pseudo Jahn-Teller distorted ground state, *J. Phys. Chem. Solids* **51**, 189 (1990).
- [37] T. Appadurai, S. Chaure, M. Mala, and A. K. Chandiran, Role of copper in enhancing visible light absorption in $\text{Cs}_2\text{Ag}(\text{Bi}, \text{In}, \text{Sb})\text{Cl}_6$ halide double-perovskite materials, *Energy Fuels* **35**, 11479 (2021).
- [38] T. Appadurai, R. Kashikar, P. Sikarwar, S. Antharjanam, B. R. K. Nanda, and A. K. Chandiran, Manipulation of parity and polarization through structural distortion in light-emitting halide double perovskites, *Commun. Mater.* **2**, 68 (2021).
- [39] Y. M. Bosworth and R. J. H. Clark, Intensity studies on the Raman-active fundamentals of hexahalogeno-anions of second- and third-row transition and non-transition metals. The calculation of parallel and perpendicular bond polarisability derivatives, *J. Chem. Soc., Dalton Trans.*, 1749 (1974).
- [40] M. Burgard and J. MacCordick, Isomorphism and spectral analogies in pairs of ionic and coordination complexes of SbCl_5 , *Inorg. Nucl. Chem. Lett.* **6**, 599 (1970).
- [41] M. A. Hooper and D. W. James, Vibrational spectra of some group Vb halides. III. A far-infrared and Raman spectral study of some hexahalogeno-, pentahalogeno-, and tetrahalogeno-bismuthate(III) and -antimonate(III) salts, *Aust. J. Chem.* **26**, 1401 (1973).
- [42] R. J. H. Clark and M. L. Duarte, Raman, resonance-Raman, and electronic spectra of tetraethylammonium hexabromoantimonate(V) and of tetra-*n*-butylammonium hexabromoantimonate(V), *J. Chem. Soc., Dalton Trans.*, 790 (1977).
- [43] J. A. Creighton and T. J. Sinclair, Vibrational spectra of hexachloromolybdates and hexachlorotungstates: Hexachloro-anions of Mo(III), Mo(IV), Mo(V), W(IV) and W(V), *Spectrochim. Acta, Part A* **35**, 507 (1979).
- [44] B. Y. Spivakov, E. S. Stoyanov, L. A. Gribov, and Y. A. Zolotov, Raman laser spectroscopic studies of bismuth(III) halide complexes in aqueous solutions, *J. Inorg. Nucl. Chem.* **41**, 453 (1979).
- [45] J. A. Dean and N. A. Lange, *Lange's Handbook of Chemistry* (McGraw-Hill, New York, 1999).